Jamil *et al.*
Journal of Analytical Science and Technology (2022) 13:54
https://doi.org/10.1186/s40543-022-00363-0

Journal of Analytical Science and Technology

RESEARCH ARTICLE

Open Access

Gold nanoparticles loaded on TiO_2 nanoparticles doped with N_2 as an efficient electrocatalyst for glucose oxidation: preparation, characterization, and electrocatalytic properties

Yasmin M. S. Jamil[1], Mohammed Ahmed Hussein Awad[2], Hussein M. A. Al-Maydama[1], Ahmed N. Alhakimi[3,4*], Mohamad M. E. Shakdofa[5] and Samir Osman Mohammed[4,6,7]

Abstract

A powder of titanium oxide nanoparticles (TiO_2 NPs) was synthesized in this study by anodizing in 0.7 M $HClO_4$ and then annealing in N_2 at 450 °C for 3 h to produce TiO_2 NPs-N_2 powder as a catalyst. These TiO_2 NPs-N_2 nanoparticles were then encrusted with Au nanoparticles utilizing the photodeposition procedure with tetrachloroauric acid ($HAuCl_4$) and isopropanol as sacrificial donors. With a surface area of 121 m^2g^{-1}, the Au NPs/TiO_2 NPs-N_2 powder catalyst has a high surface area, according to the Barrett–Joyner–Halenda technique. According to X-ray diffraction (XRD) analysis, TiO_2 NPs-N_2 contained uniformly integrated Au nanoparticles with an average crystallite size of about 26.8 nm. The XRD patterns showed that the prepared Au NPs/TiO_2 NPs-N_2 were crystallites and nano-sized. The transmission electron microscopy image revealed the spherical shape of the nanoparticles and their tendency for agglomeration. Utilizing the cyclic voltammetry, the electrochemical properties of the catalyst TiO_2 NPs powders in a basic glucose solution were investigated. The electrocatalytic activity and stability of the loaded Au NPs/TiO_2 NPs-N_2 powder on the working electrode for the electrocatalytic oxidation of glucose were astonishingly high. The Au NPs/TiO_2 NPs-N_2 catalyst demonstrated electrocatalytic characteristics that were superior to a commercially available polycrystalline gold electrode in the application involving glucose alkaline fuel cells.

Keywords: TiO_2 nanoparticles, Anodization, Photodeposition, Gold nanoparticles, BET surface area, Glucose oxidation of gold, Cyclic voltammetry

Introduction

One of the drawbacks of using TiO_2 is the rapid recombination of the induced electron–hole in the surface of TiO_2. Several studies were conducted to address this surface problem of TiO_2 using some noble metals such as gold, platinum, silver, and palladium. These metals greatly enhance surface activity by reducing the electron–hole recombination process on the surface of the noble metal–TiO_2 composite (Chen et al. 2013; Noothongkaew et al. 2017; Wang et al. 2019).

The Au/TiO_2 nanocomposite has attracted researchers due to its several applications in different aspects. A survey article about the applications of Au-loaded TiO_2 nanoparticles in water pollutant removal revealed the efficacy of these nanoparticles to remove contaminants from wastewater, groundwater, and surface water (Ayati

*Correspondence: A.Alhakimi@qu.edu.sa; alhakemi10@yahoo.com

[3] Department of Chemistry, College of Science, Qassim University, Buraidah 51452, Saudi Arabia
Full list of author information is available at the end of the article

Springer Open

© The Author(s) 2022. **Open Access** This article is licensed under a Creative Commons Attribution 4.0 International License, which permits use, sharing, adaptation, distribution and reproduction in any medium or format, as long as you give appropriate credit to the original author(s) and the source, provide a link to the Creative Commons licence, and indicate if changes were made. The images or other third party material in this article are included in the article's Creative Commons licence, unless indicated otherwise in a credit line to the material. If material is not included in the article's Creative Commons licence and your intended use is not permitted by statutory regulation or exceeds the permitted use, you will need to obtain permission directly from the copyright holder. To view a copy of this licence, visit http://creativecommons.org/licenses/by/4.0/.

et al. 2014). In relation to the effect of loading Au on TiO_2 on its photoelectric characteristics, it was discovered that doping the surface of TiO_2 nanotubes with gold nanoparticles increased the photoelectron density and promoted the photoconversion process of the TiO_2 NTs. This is due to the fact that the deposited gold nanoparticles do not change the energy gap value of titanium dioxide significantly. The energy interaction between the photon and the conduction electrons takes place in what is called the surface plasmon resonance (SPR), and this process is responsible for the photoelectric activity of the surface (Pisarek et al. 2021).

The electro-oxidation of glucose has drawn various interests because of its potential applications in a few aspects, for example, the advancement of glucose sensors and biological fuel cells (Heller and Feldman 2008; LaConti et al. 2003). There are three principles of performing glucose electro-oxidation, contingent upon the presence of dynamic oxidant agents or intermediaries: microorganism-helped oxidation, enzyme-helped oxidation, and the electronic/ionic conductor interface oxidation. Even so, there are many advantages to immediate oxidation, including easy electrode preparation, long device lifespans, and high thermodynamic productivity in fuel cell applications. It has not been well investigated, and only a few important works have addressed this topic (Abdullah and Kamarudin 2015; Hameed et al. 2022; Lertanantawong et al. 2008).

Glucose electro-oxidation was first studied in a sulfuric acid electrolyte using a lead electrode over a century ago (Corbett and Liddle 1961). Subsequently, the research efforts were focused on electrocatalytic surfaces, and then, an understanding of the oxidation mechanism was achieved (Burke and Nugent 1998; Burke and Nugent 1997; Jin and Chen 2007; Zhou et al. 2009). From those preliminary investigations, it was determined that the reaction depends surprisingly on the electrode materials and the crystallite orientation of their surfaces. Glucose oxidation on a gold electrode was explained by means of the polarization method, cyclic voltammetry (Burke and Nugent 1998; Jin and Chen 2007; Zhou et al. 2009), and massive amplitude Fourier transformed alternating current voltammetry, currently (Wang et al. 2010). It has been demonstrated that, among extraordinary substances, glucose oxidation is most energetic in alkaline solutions (Burke and Nugent 1997). Furthermore, it has been demonstrated that the electrolyte solution's pH and chemical makeup have a significant impact on gold activity. The ability of gold to oxidize glucose in a weak alkaline solution ($7 < pH \leq 10.5$) depends, in particular, on the presence of an appropriate buffer solution (Zhou et al. 2009). Neither result is obtained by employing diluted alkali. The main point from the pronounced studies was that the function of the buffer's compounds (either phosphate or carbonate) is not merely pH stabilization due to their interaction with the sugar unit. At higher pH 11, due to the presence of KOH, gold is moderately energetic, and the dependence of the oxidation reaction on the pH was investigated (Burke and Nugent 1997). The oxidation of glucose in sturdy alkaline media is especially interesting in sugar-fed fuel cells (Martins et al. 2020). The chemical instability of glucose during oxidation at high pH levels and its kinetics of degradation, on the other hand, have been extensively studied in recent years (Janitabar Darzi and Bastami 2022). This shows the formation of complex mixtures of high-and-low-molecular-weight carboxylates and aldehydes in place of simple gluconate.

Based on earlier research on the electrocatalytic and oxidation behavior of gold in aqueous solutions (Antić et al. 2012; Xu et al. 2008), the underlying methodology of glucose electro-oxidation on a gold electrode entails a fast adsorption process of glucose on the electrode, followed by dehydrogenation and degradation, in parallel, of the organic molecule (Burke and Nugent 1997). The oxidative maximum during the cathodic examination (Jin and Chen 2007; Zhou et al. 2009) was described by considering the location of oxygen anions desorbed from the metallic surface (Zhou et al. 2009), and this was an exciting feature of glucose voltammograms on gold. Recently, a number of studies have focused on improving the overall performance of gold electrodes through chemical and morphological alteration for use in fuel cells or glucose sensors (Antić et al. 2012; Govindaraj et al. 2014; Lazar et al. 2020). At moderately alkaline pH levels, modified gold nanoparticles were found to have the best glucose oxidation efficiency (Winjobi et al. 2010).

In order to demonstrate the potential of those nanostructured electrodes as anodic catalytic materials in glucose alkaline fuel cells (GAFC), this work aims to examine the morphology and structure of Au NPs supported on TiO_2 nanoparticles, analyze the electrocatalytic performances of gold nanoparticles on glucose oxidation in alkaline solutions, and compare the results with those of industrial polycrystallite gold.

Experimental

Materials

All chemicals used in this work were as follows: Ti foils (> 99.5% purity, Alfa Aesar, thickness: 0.25 mm), perchloric acid $HClO_4$ (Perchloric acid 70% $HClO_4$, MERCK, Germany), tetrachloroauric acid ($HAuCl_4$, Sigma–Aldrich, 99.9+ %) as a precursor, isopropanol (99.0%) as a sacrificial donor (Winlab, Laboratory Chemicals Reagent, Fine Chemicals), Nafion (5 wt%), Flakes Extra Pure KOH (LOBA Chemie, Laboratories reagents and Fine Chemicals, India), glucose anhydrous, $C_6H_{12}O_6$ (99% purity,

Sigma–Aldrich), titanium foils (> 99.5% purity, from Alfa Aesar, thickness: 0.25 mm), and Pt foil (99.99% purity, Sigma–Aldrich).

Synthesis of TiO_2 nanoparticles powder

The anodization process was used to create titanium oxide nanoparticles powder (TiO_2 NPs powder). The titanium foils were anodized in an aqueous solution comprising 0.7 M perchloric acid ($HClO_4$) by using a two-electrode polypropylene electrochemical cell, which consists of Ti foil as the anode and Pt foil as the cathode, at 20 V for 1 h at room temperature. TiO_2 NPs powder was formed and then separated from the solution using a centrifuge. It was then dried in an oven at 80 °C overnight. An annealing was performed for TiO_2 NPs powder in a nitrogen atmosphere at 450 °C with rates of 5 °C min^{-1}, and then, the sample was cooled in the same condition and at the same rate. Finally, TiO_2 NPs-N_2 powder was obtained.

Synthesis of Au NPs/TiO_2 NPs-N_2 catalyst using photodeposition method

In a glass beaker, 10 mM $HAuCl_3$ and 0.3 M isopropanol were combined with 150 mg of the catalyst TiO_2 NPs-N_2, which was then exposed to a 400 W UV lamp for two hours while being stirred magnetically. Utilizing an instrument from (Thorlabs), the wavelength and power used during experiments were measured and were 380 nm and 39 mW. The color of the solution changed noticeably from yellow to white when exposed to radiation in the case of Au photodeposited on TiO_2 NPs-N_2, providing proof that the metal has been adsorbed onto the powder's surface.

After photodeposition, the resulting powder (Au NPs/TiO_2 NPs-N_2) was removed from the solution using centrifugation. This powder was then cleaned with DI water and dried at 80 °C overnight. To make the ink, combine 50 mg of Au NPs/TiO_2 NPs-N_2 powder with 1 mL of D.I water and 10 L of 0.5 wt.% Nafion and homogenize them with an ultrasonic bath.

Physicochemical Characterizations

The chemical structure of the prepared materials was analyzed using energy-dispersive X-ray (EDX), Vantage 4105, NORAN.

The transmission electron microscopy (TEM) images were obtained using a TEM system from JEOL, the JEM-2100F, operating at 200 kV.

The XRD patterns (intensity versus 2θ) were recorded using a Rigaku Miniflex 100 X-ray diffractometer. The system was operated at a voltage of 40 kV and a current of 15 mA. The X-ray tube target was Cu-Kα ($\lambda = 1.5406$ nm). With a scanning rate of 2θ degrees per minute, the range of 2θ degrees was 5–80 degrees. For chilling the system, water flow was used at a rate of 3.7 L/min.

BET (Brunauer–Emmett–Teller) surface area and porosity measurements were carried out by N_2 adsorption at 77.3 K using a Quantachrome instrument.

Electrochemical measurements

Using a computerized potentiostat/galvanostat (Autolab, FRA2, AUTOLAB, TYPE III), cyclic voltammetry (CV) was carried out in a typical three-electrode single-compartment Pyrex glass cell. SCE and pure Pt foil were used as the reference and auxiliary electrodes, respectively. The SCE electrode is the sole basis for all potentials given in the text. Both a saturated calomel reference electrode (SCE) and a Pt wire auxiliary electrode were utilized. Additionally, a 3-mm Pt polycrystallite working electrode was utilized (with a geometric surface of 0.07 cm^2). NOVA 1.9 was the computer application used to conduct the cyclic voltammetry tests.

Material characterization

Using an inductively coupled plasma spectroscopy system, the mass loading of the (metal) Au NPs on the produced materials (TiO_2 NPs-N_2) was calculated (ICPS-7000 ver.2 Shimadzu, SEQUENTIAL PLASMA SPECTROMETER). Samples were dissolved in aqua regia acid using a high-pressure microwave digestion device in a Teflon tube vessel (MARSX; CEM) at 450 K and 170 psi to make the diagnosis. It made use of the Microwave Accelerated Reaction System (MARS).

Results and discussion

Physicochemical characterization of the Au NP/TiO_2 NPs-N_2 catalyst

Energy-dispersive X-ray diffractive (EDX) analysis

The chemical elements contained in the prepared materials were discovered by EDX analysis and are shown in Fig. 1. From the EDX spectra, it is evident that there are

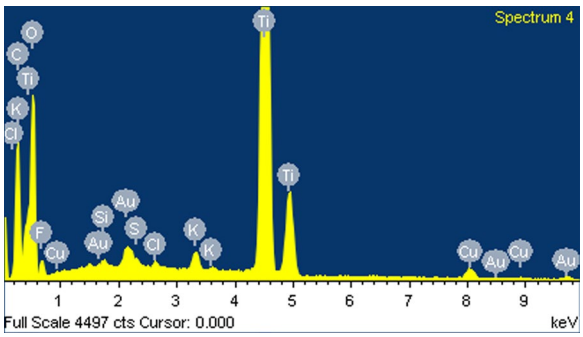

Fig. 1 The chemical elemental analysis results of the Au NPs/TiO_2 NPs-N_2 sample using EDX

no other peaks other than C, O, F, Si, S, Cl, K, Ti, Cu, and Au elements. As it can be seen, the real metal content in the samples was lower than the nominal content (10 mM $HAuCl_3$) indicating a partial reduction of the metal precursor during the photochemical deposition process carried out under the experimental conditions of this work (Senthilkumar et al. 2017). However, it is well known that EDX cannot detect elements with a lower atomic number, such as nitrogen ($Z=7$) (Yedra et al. 2021). The average values of the EDX shown in Table 1 indicate the deposition of gold nanoparticles on TiO_2 nanoparticles. In Fig. 1, the peaks of the titanium (Ti) element were observed at 0.5 keV, 4.5 keV, and 5 keV. The peaks of the gold element were observed at 1.7 keV, 2.2 keV, 8.5 keV, and 9.7 keV. These indicate the presence of Au nanoparticles and TiO_2 nanoparticles.

Size and morphology

The TEM images in Fig. 2 prove the formation of the TiO_2 NPs-N_2 powder catalyst without varying the original morphology of TiO_2 NPs. The TiO_2 NPs-N_2 average particle size measured from the TEM image is 12.01 ± 2.39 nm, showing good agreement with the XRD result (7.8 nm). TEM's images show the spherical shape with some square edges of the TiO_2-N_2 nanoparticles.

Figure 3 displays a typical TEM image of Au NPs/TiO_2 NPs-N_2 powder. The majority of Au NPs/TiO_2 NPs-N_2 is a spherical shape, demonstrating that the catalyst is formed without changing the TiO_2 nanoparticles' natural morphology. Additionally, the images support the size of gold nanoparticles that have formed. It has been observed that the majority of Au NPs are rounded and agglomerated on the TiO_2 NPs-N_2 (Moon et al. 2020; Smart and Moore 2012). The average particle size Au NPs/TiO_2 NPs-N_2 powder measured from the TEM image using ImageJ and Origin software is 23.18 ± 4.39 nm, showing consistency with the XRD outcome (26.8 nm).

From Fig. 3b, it seems that the gold incorporated in the lattice of TiO_2 was in between or beneath the TiO_2 nanoparticles. So, it can be concluded that the darker particles indicate Au nanoparticles, while the lighter dark particles are TiO_2 nanoparticles. The Au NPs/TiO_2 NPs-N_2 sizes vary between 15 and 35 nm, and it is 23.18 ± 4.39 nm. From that, it can be concluded by using the average size of TiO_2 NPs-N_2 that the average size of Au nanoparticle be concluded 11.08 nm (Buso et al. 2007; Cozzoli et al. 2006; Pennington et al. 2020).

Table 1 The element weight and atomic percentage of the chemical elements in the Au NPs/TiO_2 NPs-N_2 sample

Element	Weight %	Atomic %
C K	11.75	20.96
O K	40.45	54.19
F K	6.03	6.80
Si K	0.16	0.12
S K	0.21	0.14
Cl K	0.17	0.10
K K	0.65	0.36
Ti K	36.86	16.49
Cu K	1.96	0.66
Au M	1.77	0.19
Total	100%	100%

XRD analysis

The instrumental broadening impact was eliminated in the current work by employing LaB6's line broadening as a reference material, so that there is no need to calculate the instrumental broadening after this correction (Meier 2005).

There are three major types of TiO_2 crystal structures: rutile, anatase, and brookite; knowing that rutile is the most common and stable form in nature. The crystal structure of anatase and rutile is tetragonal, while the brookite has an orthorhombic structure (Landmann et al. 2012). The obtained pattern similarly verified the brookite and rutile phases' presence. The symbols A, B, and R indicate anatase, brookite, and rutile phases of TiO_2, respectively. Figure 4a displays the TiO_2 NPs-N_2 X-ray diffraction patterns that were captured. Major peaks at 2θ of approximately 25.491° and 54.30°, which are the peaks of the anatase A(101) and A(105), are visible in the XRD study. Furthermore, the XRD examination reveals minor peaks at approximately 27.57°, 36.29°, 37.98°, 48.22°, 62.99°, 69.18°, 75.16°, and 82.83°, which correspond to the R(110), R (102), A(004), A(200), A(204), A(220), A(301), and A(303) facets, respectively, of TiO_2 NPs-N_2. The average crystallite size of TiO_2 NPs-N_2 was calculated using Scherrer equation and found to be 7.8 nm by X-ray diffraction as in Table 2. The diffraction patterns of the synthesized anatase phase TiO_2 nanoparticles have the two most observable and strong diffraction peaks detected at 2θ equal to 25.5° (101) and 48.2° (200). According to the XRD patterns, the Au NPs/TiO_2 NPs-N_2 prefer orientation A(111). However, the prepared sample TiO_2 NPs-N_2 has the preferred orientation (101), according to the TiO_2 anatase phase (JCPDS card no. 21-1272) (Xu et al. 2008).

Actually, there was no special peak related to N_2 in the XRD pattern. The existence of nitrogen inside the crystallite lattice of TiO_2 shows a slight effect on the XRD peaks. By comparing the XRD peak positions of the reference (JCPDS card no. 21-1272) with the prepared samples, a shift was found in every peak position. This shift in peak position can be explained by the fact that doped nitrogen

Table 2 Crystallite size calculations of TiO_2 NPs-N_2 using Scherrer equation

Plane(hkl)	2θ	θ (rad)	Cos (θ) rad	FWHM (deg)	β = [FWHM] (rad)	Scherrer *D* (nm)	*D* average (nm)
A(101)	25.49	0.223	0.9999925	0.87	0.0151	9.181	7.8
R(110)	27.57	0.241	0.9999912	0.53	0.0093	14.993	
B(211)	30.89	0.269	0.9999889	0.85	0.0148	9.349	
R(102)	36.29	0.317	0.9999847	0.64	0.0112	12.416	
A(004)	37.98	0.331	0.9999833	1.21	0.0211	6.567	
B(302)	46.06	0.402	0.9999754	0.77	0.0134	10.320	
A(200)	48.22	0.421	0.9999730	0.83	0.0145	9.574	
A(105)	54.30	0.474	0.9999658	1.95	0.0340	4.075	
A(204)	62.99	0.549	0.9999539	2.73	0.0477	2.911	
A(220)	69.18	0.604	0.9999445	2.35	0.0410	3.382	
A(301)	75.16	0.656	0.9999345	1.71	0.0299	4.647	
A(303)	82.83	0.723	0.9999204	1.28	0.0223	6.209	

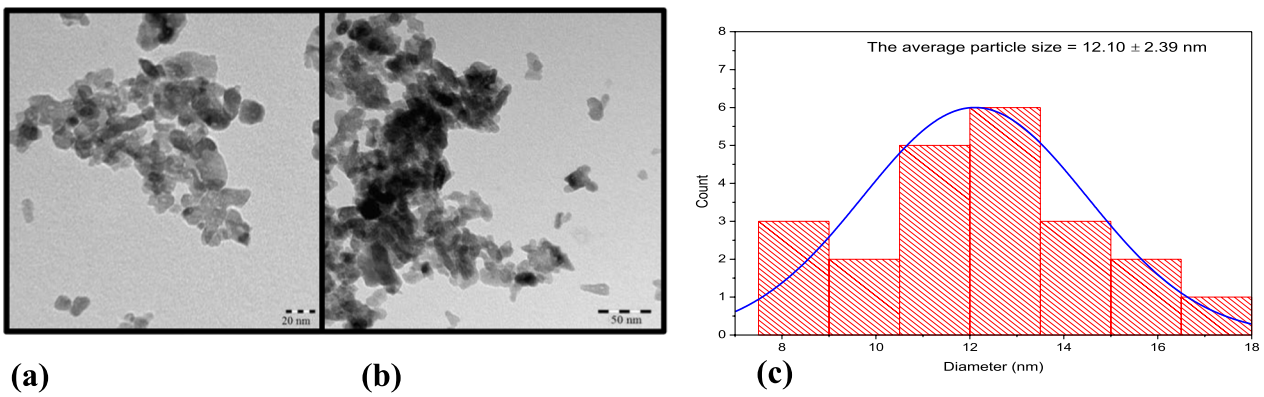

Fig. 2 TEM images of TiO_2 NPs-N_2 powder **a** at 20 nm and **b** at 50 nm and **c** corresponding particle size distribution histograms of TiO_2 NPs-N_2. The Au NPs/TiO_2 NPs-N_2 sizes vary between 15 and 35 nm, and it is 23.18 ± 4.39 nm. From that, it can be concluded by using the average size of TiO_2 NPs-N_2 that the average size of Au nanoparticles is around 11.08 nm

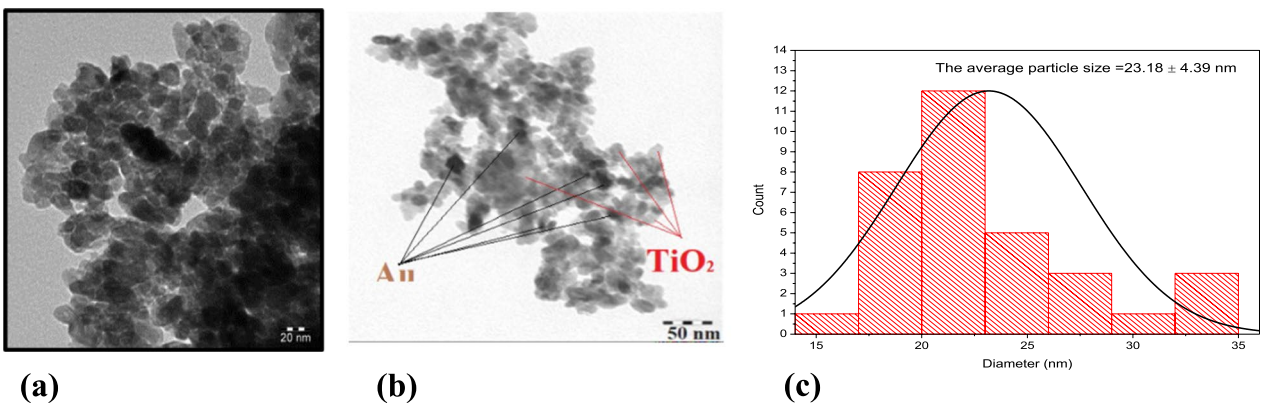

Fig. 3 TEM images of Au NPs/TiO_2 NPs-N_2 powder **a** at 20 nm and **b** at 50 nm and **c** corresponding particle size distribution histograms of Au NPs/TiO_2 NPs-N_2 catalyst

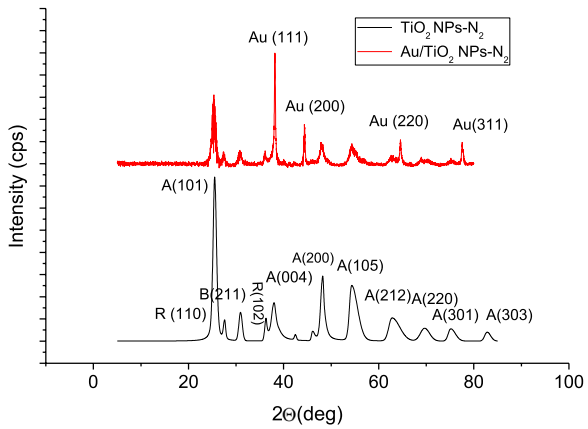

Fig. 4 XRD pattern of TiO_2 NPs-N_2 and Au nanoparticles supported on TiO_2 nanoparticles annealed in ambient of nitrogen

takes the place of oxygen atoms and slightly deforms the lattice parameters. This also led to the change in the crystal size of TiO_2. This explanation was ascertained from the previous studies on TiO_2 or metal-oxide nanoparticles. This also led to the change in the crystal size of TiO_2 (Ntozakhe et al. 2019; Theivasanthi and Alagar 2013; Valour et al. 2016; Yuan et al. 2010).

In order to quantify the particle size effects, we can estimate the mean crystallite size (D) of these samples by applying the Scherrer equation as in Ref (Kibasomba et al. 2018). The average crystallite size of the TiO_2 NPs-N_2 at the strongest (101) plane diffraction peak ($2\theta = 25.491°$) is 9.2 nm.

The X-ray diffraction patterns of the Au NPs/TiO_2 NPs-N_2 are shown in Fig. 4b. The occurrence of four different high diffraction peaks at 38.18°, 44.43°, 64.52°, and 77.55°, respectively, indexing the Bragg's reflection planes (111), (200), (220), and (311) (JCPDS No. 04-0784) (Wang et al. 2012) confirmed the face-centered cubic (FCC) of metal gold structure. The average crystallite size of Au NPs/TiO_2 NPs-N_2 was found to be 17.41 ± 1.7 nm (see Table 3), and the crystallite size of Au nanoparticle can be calculated based on the crystallite size of TiO_2 NPs-N_2 and the Debye–Scherrer formula as follows $D = \frac{K\lambda}{\beta Cos\theta}$, where K is constant (0.9) (shape factor, dimensionless factor), **D** is the mean crystal size (D is the average crystallite domain size perpendicular to the reflection planes) or grain size, λ is the wavelength of the x-ray (1.5406 A°), β is the full width at half maximum of the peak (rad) (FWHM), and θ_{max} is the Bragg angle (rad) of Au (200) or θ is the diffraction angle. It was found to be 9.61 nm.

The XRD results clearly show that Au NPs were formed by the reduction Au^+ ions to Au NPs and revealed the spherical structure of Au NPs and the high peaks indicate the energetic gold composition and crystallite nature of the Au NPs. The compound is steady, which is confirmed by its angle values (Sirdeshmukh et al. 2006).

Comparing TiO_2 NPs-N_2 to Au NPs/TiO_2 NPs-N_2, the crystal size of TiO_2 increased after Au deposition. It can be said that the incorporation of Au NPs into the crystal lattice of TiO_2 enhanced the crystallinity of the lattice, while the crystal structures of both Au and TiO_2 (two phases: anatase and rutile) kept their form. The size of the pores inside the TiO_2 structure enhances the possibility of this hypothesis. The crystal size of the nanocomposite (Au NPs/TiO_2-N_2 NPs) increased as a result (Permana et al. 2022; Romero-Torres et al. 2018).

On the other hand, those some new XRD peaks, appeared at $2\theta = 38.2°$, 44.4°, 64.52° and 77.546, were evidence for the formation of Au NPs on the TiO_2 NPs-N_2 compared with that of TiO_2 NPs-N_2, ascribing to the diffraction peaks of (111), (200), (220) and (311) planes of Au NPs/TiO_2 NPs-N_2, respectively, and the lattice constant computed from the diffraction peak (111) is a = 4.0803 Å (Wang et al. 2012).

Table 3 Crystallite size calculations of Au NPs/TiO_2 NPs-N_2 using Scherrer equation

Plane (hkl)	2θ	θ (rad)	Cos (θ) rad	FWHM (deg)	β = [FWHM] (rad)	Scherrer D (nm)	D average (nm)
A(101)	25.35	0.221	0.9999925	0.58	0.0101	13.692	17.41
R(110)	27.39	0.239	0.9999913	0.47	0.0082	16.896	
R (101)	35.94	0.314	0.9999850	0.41	0.0072	19.369	
A(200)	47.85	0.418	0.9999734	1.11	0.0194	7.154	
A(105)	54.30	0.474	0.9999658	1.80	0.0314	4.412	
A(204)	62.69	0.547	0.9999544	1.53	0.0267	5.191	
Au(111)	38.18	0.333	0.9999831	0.21	0.0037	37.816	
Au(200)	44.43	0.388	0.9999771	0.28	0.0049	28.362	
Au(220)	64.52	0.563	0.9999517	0.43	0.0076	18.469	
Au(311)	77.55	0.677	0.9999303	0.35	0.0061	22.691	

Table 4 Properties of the three major types of TiO_2 nanoparticles' crystal structures (rutile, anatase, and brookite)

Crystal system	Anatase (A) Tetragonal $a=b, V=a^2c$	Rutile (R) Tetragonal $a=b, V=a^2c$	Brookite (B) Orthorhombic $a\neq b\neq c, V=abc$
a (A°)	3.838829	4.5730	9.184
b (A°)	–	–	5.447
c (A°)	9.47136	2.9090	5.145
c/*a*	2.46725	0.6361	0.5602
V (A^{o3})	139.5757	60.83397	257.38
Coordination number-Z	4	2	8

Table 5 The inter-planer *d*-spacing TiO_2 NPs-N_2 samples of crystal structure tetragonal of TiO_2 NPs anatase and rutile phases

Plane (hkl) (Miller indices)	2*θ* (degree)	*D* Practical (A°)	*d* (Bragg) (A°)	*D* (theoretical) (A°)
A(101)	25.491	3.492	3.4924	3.4924
R (110)	27.57	3.232	3.2336	3.2336
R(102)	36.29	2.474	2.4741	2.4741
A(004)	37.98	2.367	2.3678	2.3678
A(200)	48.22	1.8858	1.8862	1.8862
A(105)	54.30	1.6880	1.6885	1.6885
A(204)	62.99	1.4744	1.47486	1.47486
A(220)	69.18	1.3569	1.35723	1.35723
A(301)	75.16	1.2630	1.26339	1.26339
A(303)	82.83	1.1644	1.16476	1.16476

From Tables 2 and 3, there are agreements between the values of crystallite size (XRD patterns) and particle size (TEM images) for TiO_2 NPs-N_2 and Au NP/TiO_2 NPs-N_2 samples.

The lattice parameters (a, b, and c) for TiO_2 NPs-N_2 with crystal system tetragonal (anatase, rutile, and brookite) were calculated as shown in Table 4, and they are almost identical to those reported in the (JCPDS anatase cards TiO_2 (No. 21-1272)) card for TiO_2.

The d-spacing values obtained from practical result, the Braggs' law ($d=(\lambda)/(2\ \sin\ \theta)$), and the theoretical ($1/d^2=\left[\left(h^2+k^2/a^2\right]+\left(l^2/c^2\right)\right)$ equations were almost identical (Table 5).

The plane *d*-spacing (*d*) related to the lattice parameters *a*, *b*, *c* and the Miller indices (*h*, *k*, *l*) were calculated by means of the theoretical ($1/d^2=\left[\left(h^2/a^2\right]+\left[\left(k^2/b^2\right]+\left(l^2/c^2\right)\right)$ and Braggs' equations ($d=\frac{\lambda}{2\sin\theta}$) (see Table 6).

The coordination number in case of tetragonal anatase system is 4 and for tetragonal rutile system is 2 and for orthorhombic brookite is 8 (Keswani et al. 2010).

The lattice parameters (*a*, *b*, and *c*) for Au NPs/TiO_2 NPs-N_2 with a face-centered cubic (FCC) crystal structure were calculated as in Table 7. The lattice parameters (*a*, *b*, and *c*) (Table 7) are almost identical to those reported in the (JCPDS 04-0784) card for Au (Ninsonti et al. 2014). The *d*-spacing values obtained from Braggs' law, and the theoretical ($d_{hkl}=a/\sqrt{(h^2+k^2+l^2)}$) equations, are almost identical (Table 7).

Table 6 The inter-planer d-spacing TiO_2 NPs-N_2 sample with brookite phase

Plane (hkl)	2*θ* (degree)	d (A°) Practical	d (A°) (Bragg)	d (A°) (theoretical)
B(110)	25.491	3.492	3.4924	3.4924
B(211)	30.89	2.893	2.8932	2.8932
B(302)	46.06	1.969	1.9695	1.9695

Table 7 Au NPs/TiO_2 NPs-N_2 lattice parameters (*a*, *b*, and *c*) and the inter-planer d-spacing

Plane (hkl)	2*θ* degree	Lattice parameters (A°)		Average Volume ($V=a^3$)	d(Å) Practical	d(A°) Bragg	d(A°) theoretical
		$a=b=c$ (FCC)	average (A°)				
Au(111)	38.182	4.0803	4.079	67.912	2.3551	2.3558	2.3558
Au(200)	44.43	4.0758			2.0375	2.0379	2.0379
Au(220)	64.52	4.0829			1.4431	1.4435	1.4435
Au(311)	77.546	4.0807			1.23004	1.2304	1.2304

Specific surface area (SSA)

The surface area plays a critical role inside the nanoparticles, due to their large surface to size ratio with a lower in particle size (Jiang et al. 2007). SSA is a material property. It is a systematic value that can be used to determine a material's nature and qualities. In the context of adsorption, heterogeneous catalysis, and surface reactions, it is particularly significant. SSA stands for each mass's surface area (SA).

According to Zhang report (Gao and Zhang 2001), as material sizes shrink, the precise surface area and surface-to-volume ratio drastically increase. Because of the high surface area of TiO_2 nanoparticles, interaction between the nanoparticles and the surrounding materials is possible. This interaction often occurs at the surface or on the interface and is highly dependent on the surface area of the material (Jiang et al. 2007). Mathematically, SSA can be computed using the following formula (Pan and Xu 2013), and the calculated data are shown in Table 8.

$$\mathrm{SSA} = 6 \times 10^3 / \mathrm{D}\ \rho$$

where SSA is the specific surface area, D is the crystallite size, and ρ is the density of nanoparticles ($\rho(TiO_2)$ anatase = 3.79 g cm^{-3} & ρ(Au) = 19.320 g cm^{-3}). From Table 8, it is noted that the average SSA for Au NPs/TiO_2 NPs-N_2 is 121 m^2/g, whereas it is 202.96 m^2/g for TiO_2 NPs-N_2.

Dislocation density

A material's unit lattice, an atom or an ion, has a liner flaw called a dislocation. The disordering of these units in an array by some mechanisms, such as the absence of atoms or the existence of impurities, results in their dislocation. For some of the material's properties, like its mechanical and electrical properties, this flaw may be more advantageous. Industrially, these changes in lattice structure may be desired according to the resultant properties. The crystallinity of the substance is related to this lattice deformation (Jamil and Fasehullah 2021).

The crystallite size and dislocation density can be computed using X-ray line profile analysis (Ungár et al. 2005). The dislocation density (δ) in the sample was calculated using the expression $\delta = 1/D^2$, and the results are shown in Table 8. The δ average of TiO_2 NPs-N_2 is 1.992×10^{16} m^{-2}, and the δ average of Au NPs/TiO_2 NPs-N_2 is 1.704×10^{15} m^{-2}.

Morphology index (MI)

It is well known that the peak broadening in the XRD pattern is due to the finite size of the particles. The width of the diffraction peaks increases with the decrease in particle size. The morphology index (MI) is used to affirm the uniformity and fineness of the prepared nanoparticles. It is calculated using the full width half maximum (FWHM) of the XRD peak. MI gives an indication that the specific surface area of TiO_2 nanoparticles relies on the interrelationships between particle morphology and size. MI is calculated as follows: $MI = FWHM_h/(FWHM_h + FWHM_p)$ (Theivasanthi and Alagar 2013), where $FWHM_h$ is the highest value of full width half maximum of XRD peaks, and $FWHM_p$ is the specific value of full width half maximum of a peak where the MI has to be computed. These results are plotted in Figs. 5 and 6 (a and b).

The details are shown in Table 8. The MI range of TiO_2 nanoparticles is from 0.50 to 0.82, and the MI range of Au NPs/TiO_2 NPs-N_2 is from 0.5 to 0.67. It is discovered that MI is, with a minor variation, directly proportional to particle size and inversely proportional to exact surface area. The deviations and relationships between them are indicated by the linear fit within the

Table 8 Morphology Index, specific surface area, and dislocation density of Au NPs/TiO_2 nanoparticles

Plane (hkl)	2θ	Scherrer *D* (nm)	Specific Surface Area (SSA) (m^2/g)	Morphology Index (MI) (unit less)	Dislocation Density (δ) (m^{-2}) × 10^{15}	Average (δ) (m^{-2})
A(101)	25.35	13.692	115.929	0.756	5.33	1.992×10^{16}
R(110)	27.39	16.896	83.951	0.793	3.50	
R (101)	35.94	19.369	73.233	0.815	2.67	
A(200)	47.85	7.154	221.876	0.619	19.54	
A(105)	54.30	4.412	359.769	0.500	51.37	
A(204)	62.69	5.191	305.779	0.541	37.11	
Au(111)	38.182	37.816	8.2124	0.672	0.699	1.704×10^{15}
Au(200)	44.43	28.362	10.9498	0.606	1.24	
Au(220)	64.52	18.469	16.8152	0.500	2.93	
Au(311)	77.546	22.691	13.6864	0.551	1.94	

figure. The uniformity and fineness of the prepared nanoparticles are confirmed by the MI results.

Nitrogen adsorption and desorption isotherm of Au NPs/TiO_2 NPs-N_2

The mesoporous TiO_2 materials are extensively used in a variety of applications, including the loading of pharmacological molecules, proteins, nucleic acids, and other biological macromolecules for tumor multimodal treatment. Additionally, these nanomaterials have the capacity to store energy and safeguard the environment through processes including the photocatalytic destruction of pollutants, the production of photochemical fuel, the photoelectrocatalytic separation of water, and catalyst support (Tahir et al. 2015; Zhang et al. 2014).

The prepared samples' nitrogen adsorption–desorption isotherms and associated pore size distribution are shown in Fig. 7. As shown, the sample has the characteristics of a mesoporous material, including progressive adsorption–desorption hysteresis, denoted by type IV isotherms. This type contains complex pore systems, called inkbottle-shaped pore networks. The broader pore body remains filled until a lower pressure is attained, at which point the neck evaporates, delaying the pore evaporation, which no longer happens via equilibrium in an open pore (Jinga et al. 2021; Shelyapina et al. 2022). Table 9 provides a summary of the variations in BET surface area, average pore size, and pore volume following Au photo-desorption. After Au NP was adsorbed, it was discovered that the average pore diameter decreased. Due to the slight pore obstruction caused by the deposited Au NPs on TiO_2 NPs-N_2, the BET surface area and average pore decreased (Ismail et al. 2009; Kim et al. 2013).

The P/P° range of 0.67 to 0.99 reveals a sharp rise in the adsorption volume of N_2. As well as, it is clear that the range 0.6 to 0.98 P/P° exhibits a capillary condensation step. Nitrogen adsorption–desorption isotherms of Au NPs/TiO_2 NPs-N_2 powder are displayed in Fig. 7 and are expressed as a function of relative pressure (P/P°) versus cc/g (Volume at STP) (N_2-physisorption isotherm). The BET surface area of the sample Au NPs/TiO_2 nanoparticles is 84.6 m^2/g, and the total pore volume is 0.259 cm^2/g. Its bimodal pore size distribution exhibits highest values at 5.42 and 7.31 nm, respectively. For effective electrolyte diffusion into the photoanode in dye-sensitive solar cells (DSSC), this type of porous construction can be helpful (Govindaraj et al. 2014).

The nitrogen adsorption and desorption isotherms shown in Fig. 7 were used to calculate the specific surface area and porosity of the mesoporous Au NPs/TiO_2 NPs-N_2. The stepwise adsorption and desorption branch of the type IV pattern is revealed by the sample's isotherm, showing the presence of mesoporous material with a three-dimensional (3D) intersection according to the IUPAC classification (Jinga et al. 2021). The material that was produced has a broader mesoporous structure, according to this result. Table 10 gives the summary of Barrett–Joyner–Halenda (BJH) adsorption data.

The average pore diameter, determined through the BJH method using the adsorption isotherm, is presented in Table 11.

As shown in Fig. 8, the adsorption branch of the BJH approach was used to explore the plots of the pore size distribution in order to look at pore size. The mesoporous Au NPs/TiO_2 NPs-N_2 have 4.61 nm and 5.42 nm average pore sizes. The BJH technique resulted in a pore size distribution (Fig. 8) that is clearly narrow (5.42 nm), indicating high sample quality. In the desorption branch, it is discovered that the samples form a type IV isotherm with a type H_2 hysteresis loop (low order) close to a relative pressure of 0.50, which is associated with abrupt capillary condensation occurring in

Table 9 The average BET surface area, average pore size, and pore volume of Au NPs/TiO_2 NPs-N_2 powder

Sample	BET surface area (m^2/g)	BJH adsorption summary surface area (m^2/g)	Average pore size (Pore diameter) dv(d) (nm)	Pore volume (cm^3/g)
Au NPs/TiO_2 NPs-N_2	84.6	121.128	5.420	0.259

Table 10 BJH adsorption summary

Nanostructure	Surface Area (m^2/g)	Pore volume (cc/g)	Pore Diameter dv (d) (nm)
Au NPs/TiO_2 NPs-N_2	121.128	0.259	5.420

Table 11 The average pore diameters of the sample using the BJH method

Bimodal	ds(d) m^2/nm/g		dv(d) cc/nm/g	
	Diameter (nm)	m^2/nm/g	Diameter (nm)	cc/nm/g
Au NPs/TiO_2 NPs-N_2 powder	3.01	22.1	3.01	0.0166
	3.71	20.4	3.71	0.0189
	4.61	21.1	4.61	0.0243
	5.42	19.2	5.42	0.0260
	7.31	11.2	7.31	0.0205
	9.31	7.97	9.31	0.0186

mesoporous (Wu et al. 2009). Pore diameter (nm) versus dv(d) cc (nm/g), or pore size distribution, is used to express nitrogen adsorption–desorption isotherms of Au NPs/TiO_2 NPs-N_2 powder (as shown in Fig. 9a and b). The BJH technique resulted in a pore size distribution that is clearly narrow (3.16 nm) and confirms the high quality of the material.

Electrochemical characterization

Electrochemical tests were performed in (2 M KOH + 0.1 M glucose). The solution of 7 µL of Au NPs / TiO_2 NPs-N_2 crystallite powder contains 0.05145 mg Au, which was loaded onto the electrode with a micropipette.

Glucose oxidation of Au NPs/TiO_2 NPs-N_2 powder

From Fig. 10, the cyclic voltammetry (CV) curve of the Au NPs/TiO_2 NPs-N_2 electrode in an alkaline solution of glucose indicates three clear electrochemical processes through the anodic sweep and one through the cathodic return scan.

At the peak "$a = -0.59$ V," numerous authors have described it as the region of dehydrogenation of anomeric carbon within adsorption process (Grochowska et al. 2019; Ouyang et al. 2013). This dehydrogenation of the anomeric carbon peak was confirmed by the examination of a platinum electrode (Ernst et al. 1980; Largeaud et al. 1995). The tests demonstrated the maximum energetics on the electrode surface of CV, which indicates the stability of the beta-D-glucose anomer due to its planar molecules. Moreover, it is significant to note that this peak shifts almost −0.6 V in the direction of lower potential with reference to the polycrystallite platinum. The higher oxidation potential on Pt is almost certainly attributable to the hydrogen adsorption that competitively hinders glucose adsorption; this phenomenon is negligible on the gold surface.

Figure 10 shows the second region at peak "$b = 0.1$ V." This peak is wider than previous ones, with a large left shoulder due to several oxidative strategies going on in the potential range from −0.3 to 0.2 V. The techniques on a Pt electrode at low temperature (2 °C) were defined, and it was pointed out that the oxidation of the previously adsorbed intermediate follows two probable paths. At $E < 0.1$ V, it is oxidized as weakly adsorbed gluconate, either connected via two or merely one oxygen. At the second rout, $0.1 < E < 1.1$ V, where glucose is oxidized as weakly adsorbed δ-gluconolactone. At 25 °C, it was discovered that the peak b is a convolution of several peaks, which means that in each peaks the oxidation product is constantly gluconate. Using the area under CV curve (forward scan), the charge can be obtained and then divided by scan rate and potential range, as well as the mass of the sample, and the specific capacitance can be calculated. From that, it was found that the specific energy density of glucose is equivalent to 6.64 kWh/L or 4.32 kWh/kg.

Table 12 Comparison between 7 µL Au NPs/TiO_2 NPs-N_2 powder and 0.07 cm^2 Au polycrystallite working electrode in (2 M KOH + 0.1 M glucose) at a scan rate was 50 mV/s

Electrode	I_f (mA /cm^2) of (Peak *a*)	I_b (mA /cm^2) of (Peak *d*)	$I_{f(a)}/I_{b(d)}$	Mass loading(mg)
Au NPs/TiO_2 NPs-N_2	9.37	13.8	0.679	0.05145
Au WE	8.4	12.5	0.672	–

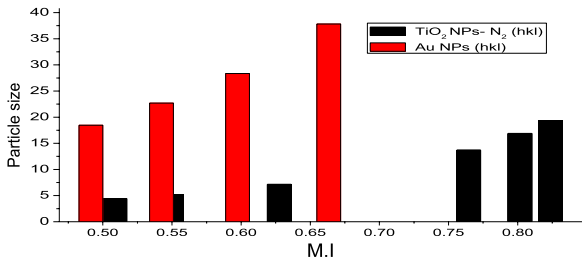

Fig. 5 Morphological index Vs particle size of Au NPs/TiO_2 nanoparticles

Around the value of 0.4 V, zone c, the gold surface oxidation occurs according to the CV curves in the presence and absence of glucose. Quartz crystal microbalance analysis combined with electrochemical equipment (Beden et al. 1996) demonstrated the formation of an Au/O species in the 0.2 V range. The glucose can be oxidized at the metal gold surface, but not on the gold oxide surface, which stops oxidation at potentials higher than 0.3 V.

In the cathodic return scan of CV, an oxidative pinnacle was observed, peak *d*, and was formerly noticed in previous studies. It is a sharp peak due to the decreasing oxide layer. Liu and Makovos were the first to explain the mechanism for oxidation through the cathodic sweep: The oxide layer is reduced to form free O_2− anions, which then react with glucose to produce gluconic acid. Following that, the Au surface is re-oxidized via OH− in solution. Using the unloaded Pt polycrystallite electrode, no electrochemical mechanisms were found in the glucose solution (Fig. 10, black line) (Hsiao et al. 1992; Xiang et al. 2003).

Au NPs/TiO_2 NPs-N_2 and commercial gold pin electrode comparison

Figure 11 shows that Au NPs particles outperform the standard Au polycrystallite electrode in terms of current density output and that the oxidation processes

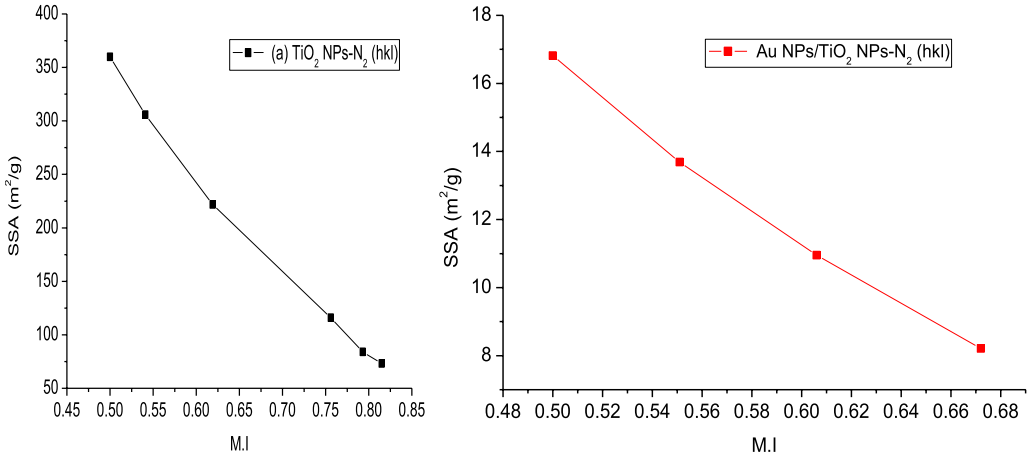

Fig. 6 MI Vs specific surface area of **a** TiO_2 NPs-N_2 (hkl) and **b** Au NPs/TiO_2 NPs-N_2 (hkl)

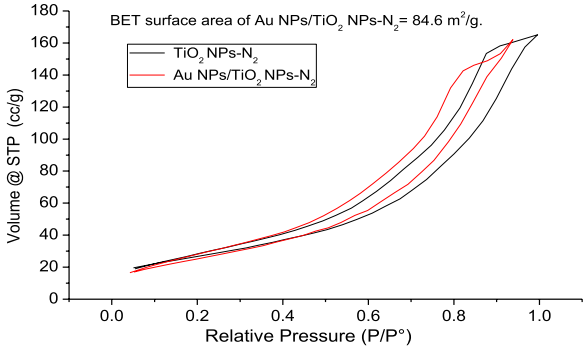

Fig. 7 Adsorption–desorption isotherm of TiO_2 NPs-N_2 and Au NPs/TiO_2 NPs-N_2 powder

shift toward lower potentials. It is crucial to stress that the current densities in both instances were calculated using the geometric surface area. It is also intriguing to note the significant increase in peak current density, as in Fig. 11, which is related to the presence of more faulty sites on the surface of gold nanoparticles. Given that surface reactions frequently demand lower activation energies when defective sites are present (such as kink atoms), the nanoparticles should naturally include a significant number of defects that are responsible for the increased oxidative adsorption of glucose (Basu and Basu 2010; Feng et al. 2009; Toles et al. 1999). The aim of the comparison is to understand the influence of the electrolyte on the generation of peak d in Fig. 11. Table 12 shows the

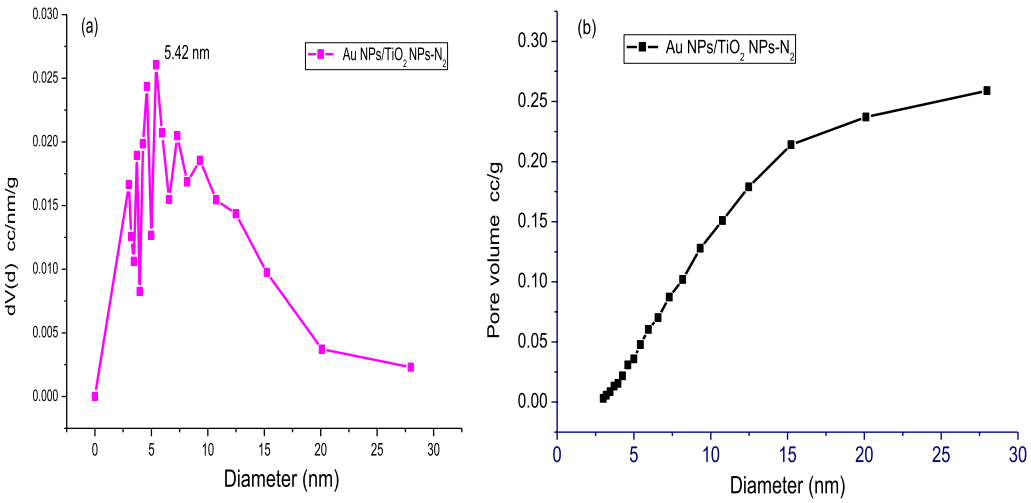

Fig. 8 **a** The average pore diameter, determined through the Barrett–Joyner–Halenda (BJH) method by the adsorption isotherm **b** diameter (nm) versus pore volume (cc/g) (volume @ STP)

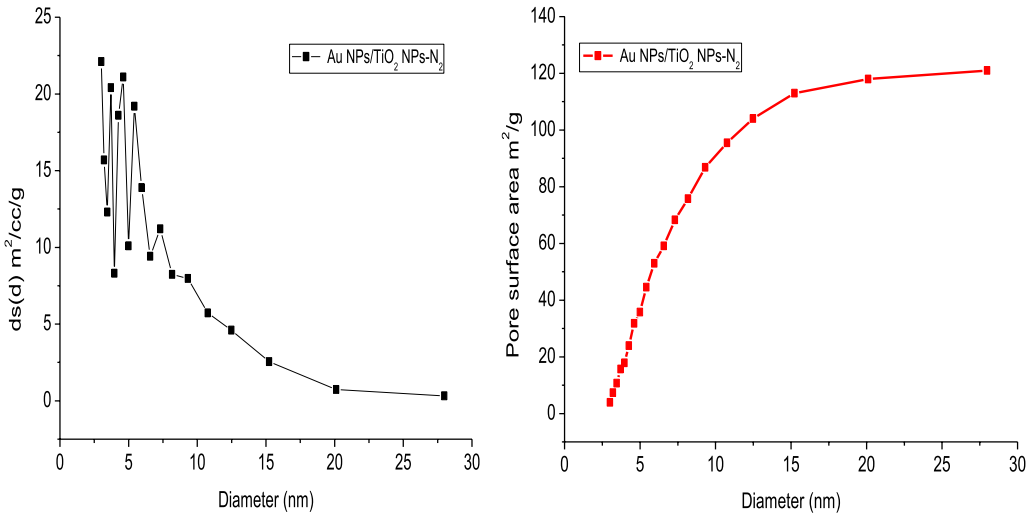

Fig. 9 **a** Diameter (nm) versus ds (d) m^2/cc/g. **b** Diameter (nm) versus pore surface area (m^2/g)

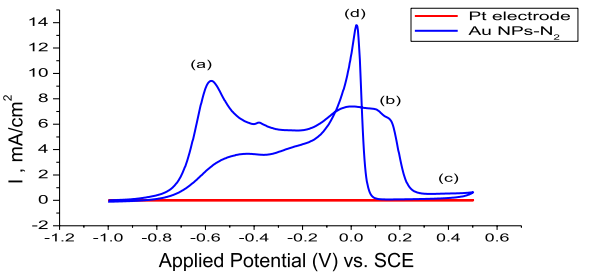

Fig. 10 CV of Pt polycrystalline electrode and Au NPs/TiO_2 NPs-N_2 in (2 M KOH + 0.1 M glucose) at scan rate was 50 mV/s by current density

comparison between 7 µL of Au NPs/TiO_2 NPs-N_2 powder and 0.07 cm^2 of Au polycrystallite working electrode in the basic solution of glucose.

Loading effect of Au NPs/TiO_2 NPs-N_2

Figure 12 demonstrates the effect of putting Au NPs/TiO_2 NPs-N_2 powder catalyst on the working electrode (3 mm diameter Pt). This investigation is to determine the optimal loading of Au NPs/TiO_2 NPs-N_2 powder. The catalytic current density clearly increased with loading quantities of 3 µL, 5 µL, and 7 µL, respectively. When the loading reaches 10 µL, the catalyst will block and physically detach, which will result in a drop in the catalytic current density. From Fig. 12, it is concluded that the number of redox sites decreases with the amount of Au NPs/TiO_2 NPs-N_2 powder. This is due to the Au NPs/TiO_2 NPs-N_2 powder fusing and clustering at loadings greater than 7 µL. Therefore, it is recommended to use loading quantities equal to or smaller than 7 µL to provide satisfactory electrochemical performance for the prepared sample (Ampelli et al. 2015; Ravishankar et al. 2017). Table 13 shows that the I_f/I_b value of the 7 µL (Au NPs/TiO_2 NPs-N_2 powder catalyst) is higher than that of the 3 µL, 5 µL, and 10 µL, and this quantity of the loaded catalyst has the highest catalytic activity and current density.

Table 13 Different loading quantity, I_p (peak height) for both the forward and backward paths, I_f/I_b the forward and backward current density at three peaks (*a*, *b*, and *d*) at scan rate was 50 mV/s

Loading (µL)	Forward direction (Peak *a*) dehydrogenation of the anomeric carbon peak		Forward direction (Peak *b*)		Backward direction (Peak *d*) oxidative peak
	I_f (mA /cm^2)	$I_{f(a)}/I_{b(d)}$	I_f (mA /cm^2)	$I_{f(b)}/I_{b(d)}$	I_b (mA /cm^2)
3 µL	3.22	0.672	1.86	0.392	4.79
5 µL	5.01	0.658	3.76	0.494	7.61
7 µL	9.37	0.679	7.25	0.525	13.80
10 µL	5.88	0.503	4.68	0.503	11.69

Table 14 The scan rate, $\sqrt{\text{scan rate}}$, I_p (peak height) for both the forward and backward paths also contains the values of I_f/I_b for the Au NPs/TiO_2 NPs-N_2 powder catalyst loaded on Pt working electrode 20 cycles in (2 M KOH + 0.1 Glucose) (GOR)

Scan (mV/s)	$\sqrt{\text{scan rate}}$ $\left(\sqrt{\frac{\text{mV}}{\text{s}}}\right)$	Forward direction (Peak a) dehydrogenation of the anomeric carbon peak		Forward direction (Peak *b*)		Forward direction (Peak *c*)		Backward direction (Peak *d*) oxidative peak
		I_f (mA/cm^2) (− 0.59 V)	$I_{f(a)}/I_{b(d)}$	I_f (mA /cm^2) (0.147 V)	$I_{f(b)}/I_{b(d)}$	I_f (mA /cm^2) at voltage (0.49 V)	$I_{f(c)}/I_{b(d)}$	I_b (mA / cm^2) at voltage 0.023 V)
10	3.162	4.77	0.556	5	0.583	0.268	0.031	8.58
20	4.472	6.21	0.580	5.50	0.514	(0.384)	0.036	10.7
50	7.071	9.37	0.679	7.25	0.525	(0.643)	0.047	13.8
75	8.660	11.1	0.745	8.56	0.575	(0.776)	0.052	14.9
100	10	12.67	0.823	9.5258	0.619	0.9360	0.061	15.398

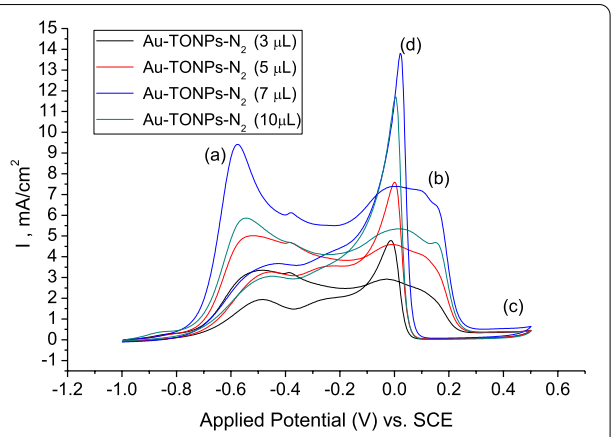

Fig. 11 CV of Au polycrystalline and Au NPs/TiO_2 NPs-N_2 in (2 M KOH + 0.1 M Glucose) at scan rate was 50 mV/s by current density

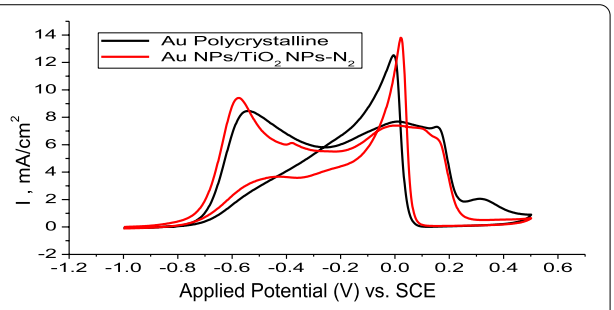

Fig. 12 (Effect of loading) CV for photodeposition of (Au supported on TiO_2 NPs-N_2) loaded on 3 mm Pt polycrystalline working electrode (conductor) in (2 M KOH + 0.1 M glucose) at a scan rate was 50 mV/s, and catalyst loading was 3,5,7 and 10 µl, 20th cycles

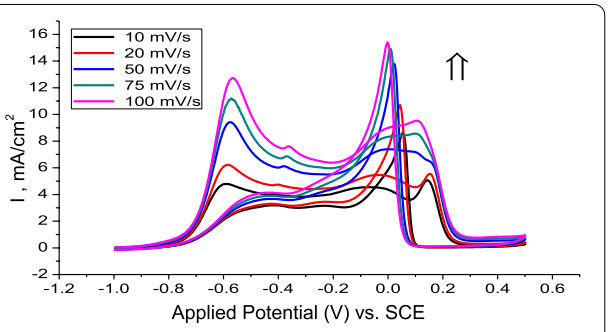

Fig. 13 CV of Au NPs/TiO_2 NPs-N_2 powder loaded on 3-mm-diameter Pt working electrode in (2 M KOH + 0.1 M glucose), 7 µl loading by current density, 20 cycles (effect of scan rate)

Scan rate effect of Au NPs/TiO_2 NPs-N_2

The experiment's scan rate (V/s), or rate of voltage change over time, is measured during each of these phases. As opposed to measuring the current between the working electrode and the counter electrode, one measures the potential between the working electrode and the reference electrode. Actually, when the scan rate increased, the electron and mass transfers accelerated. Along with the scan rate, the charging current and Faraday current both rise. The flux of concentration at the electrode surface is proportional to the faradaic current flowing through the electrode (Park et al. 2012). Positive voltage changes of the current peaks were observed in both the forward and backward scans. Oxidation reactions and the release of protons are processes happening during the forward scan. On the other hand, during the backward scan, reduction reactions

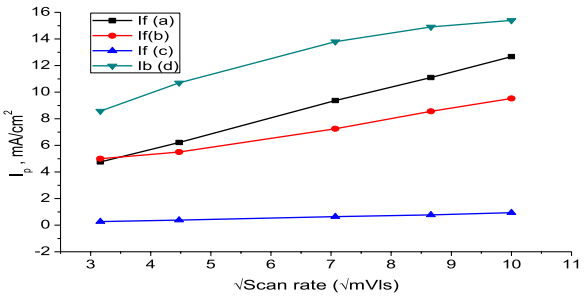

Fig. 14 I_p (peak height-mA/cm^2) versus the $\sqrt{\text{scan rate}}$ $\left(\sqrt{(mV/s)}\right)$ for both forward and backward paths of Au NPs/TiO_2 NPs-N_2 powder in (2 M KOH + 0.1 M glucose)

involving proton absorption take place (Reichert et al. 2015).

Figure 13 depicts the effect of scan rate (from 10 to 100 mV/s) for an Au NPs/TiO_2 NPs-N_2 powder electrode in the potential range of (−1 V to 0.5 V) recorded at various scan rates for 0.1 M glucose in the basic medium (2 M KOH) solution. This performance is typical of an electrochemical reaction regulated by a diffusion process.

Table 14 depicts the influence of scan rate for an Au NPs/TiO_2 NPs-N_2 powder catalyst electrode measured at various scan rates (10–100 mV/s) for a solution containing (2 M KOH + 0.1 M glucose), improved forward and backward current pathways, and the ratio I_f/I_b.

As shown in Fig. 14, there is a linear relationship between the square root of the scan rate and the cathodic forward and anodic backward peak current paths. This behavior is typical for the glucose oxidation reaction's diffusion-controlled electron transfer process.

Due to the constant diffusivity of active species, the slope will increase with increased scan rate. The higher current, as predicted by the Randles–Sevcik equation, which is inversely proportional to the square root of the scan rate, will result from this. The scan rate is inversely correlated with the charging current. Therefore, at faster scan rates, the charging current becomes comparatively more significant (Chiu et al. 2020; Jovanović et al. 2020).

Conclusions

A gold nanoparticle electrode was deposited on TiO_2 nanoparticles annealed in an N_2 electrode by the photodeposition technique of the gold medal using tetrachloroauric acid ($HAuCl_3$) and isopropanol as a sacrificial donor. The elemental quantification and stoichiometry ratio of Au NPs/TiO_2 NPs-N_2 were confirmed by EDX analysis. The TEM image of Au NPs/TiO_2 NPs-N_2 showed that the particles were spherical. The XRD pattern indicated a crystallite and face-centered cubic (FCC) structure of Au NPs/TiO_2 NPs-N_2 with an average particle size of 17.41 nm. The resulting Au NPs/TiO_2 NPs-N_2 catalyst exhibited a high surface area of 121 m^2/g. The gold nanoparticles exhibit better electrocatalytic properties than commercially available polycrystallite electrodes for glucose oxidation. Furthermore, the oxidation of sorbitol, the reduced form of glucose, showed the undertaking of the peak at −0.59 V for the anomeric carbon oxidation. A very sturdy increment in the electrode's overall performance in glucose oxidation was attained by improving the whole quantity of gold nanoparticles, which was achieved via a platinum polycrystallite electrode tip support. With this electrode, the current densities are multiplied up to 13 mA/cm^2. These effects open new possibilities for applications for gold nanoparticles in glucose alkaline fuel cells (GAFC) and glucose sensing.

Acknowledgements
Not applicable

Author contributions
YMSJ planned the project and contributed to supervision and revision. MAHA: PhD student, designed and carried out the research, practical experiments, data analysis, formal analysis of data, calculations of data, methodology, investigation, and drawing of all graphs using origin, software, and characterizations. HMAA-M planned the project and was involved in supervision and revision. ANA-H contributed to methodology, data curation, and reviewing and editing. Mohamad M.E. Shakdofa was involved in conceptualization, investigation, data processing, and revision. SOM contributed to formal analysis, resources, and editing draft. All authors read and approved the final manuscript.

Funding
There is no funding for this work.

Availability of data and materials
The datasets used and/or analyzed during the current study are available from the corresponding author on reasonable request.

Declarations

Competing interests
The authors declare that they have no competing interests.

Author details
[1]Department of Chemistry, Faculty of Science, Sana'a University, Sana'a, Yemen. [2]Chemistry Department, Faculty of Applied Sciences, Thamar University, Thamar, Yemen. [3]Department of Chemistry, College of Science, Qassim University, Buraidah 51452, Saudi Arabia. [4]Department of Chemistry, Faculty of Science, Ibb University, Ibb, Yemen. [5]Inorganic Chemistry Department, National Research Centre, 33 El-Bohouth St., P.O. 12622, Dokki, Giza, Egypt. [6]Department of Mechatronics, Faculty of Engineering, Aljanad University for Science and Technology, Taiz, Yemen. [7]Department of Physics, Physics Department, Faculty of Science, Ibb University, Ibb, Yemen.

Received: 20 September 2022 Accepted: 15 December 2022
Published online: 27 December 2022

References

Abdullah N, Kamarudin SK. Titanium dioxide in fuel cell technology: an overview. J Power Sources. 2015;278:109–18.
Ampelli C, Leonardi SG, Genovese C, Lanzafame P, Perathoner S, Centi G, et al. Monitoring of glucose in fermentation processes by using Au/

TiO_2 composites as novel modified electrodes. J Appl Electrochem. 2015;45(9):943–51.
Antić Ž, Krsmanović RM, Nikolić MG, Marinović-Cincović M, Mitrić M, Polizzi S, et al. Multisite luminescence of rare earth doped TiO_2 anatase nanoparticles. Mater Chem Phys. 2012;135(2–3):1064–9.
Ayati A, Ahmadpour A, Bamoharram FF, Tanhaei B, Mänttäri M, Sillanpää M. A review on catalytic applications of Au/TiO_2 nanoparticles in the removal of water pollutant. Chemosphere. 2014;107:163–74.
Basu D, Basu S. A study on direct glucose and fructose alkaline fuel cell. Electrochim Acta. 2010;55(20):5775–9.
Beden B, Largeaud F, Kokoh KB, Lamy C. Fourier transform infrared reflectance spectroscopic investigation of the electrocatalytic oxidation of D-glucose: identification of reactive intermediates and reaction products. Electrochim Acta. 1996;41(5):701–9.
Burke LD, Nugent PF. The electrochemistry of gold: I the redox behaviour of the metal in aqueous media. Gold Bull. 1997;30(2):43–53.
Burke LD, Nugent PF. The electrochemistry of gold: II the electrocatalytic behaviour of the metal in aqueous media. Gold Bull. 1998;31(2):39–50.
Buso D, Pacifico J, Martucci A, Mulvaney P. Gold-nanoparticle-doped TiO_2 semiconductor thin films: optical characterization. Adv Funct Mater. 2007;17(3):347–54.
Chen Y, Tang Y, Luo S, Liu C, Li Y. TiO_2 nanotube arrays co-loaded with Au nanoparticles and reduced graphene oxide: facile synthesis and promising photocatalytic application. J Alloys Compd. 2013;578:242–8.
Chiu W-T, Chang T-FM, Sone M, Tixier-Mita A, Toshiyoshi H. Roles of TiO_2 in the highly robust Au nanoparticles-TiO_2 modified polyaniline electrode towards non-enzymatic sensing of glucose. Talanta. 2020;212:120780.
Corbett WM, Liddle AM. The alkaline degradation of glucose and of some of its acetyl derivatives. J Chem. Soc. 1961;105;531–8.
Cozzoli PD, Curri ML, Giannini C, Agostiano A. Synthesis of TiO_2–Au composites by Titania-Nanorod-assisted generation of gold nanoparticles at aqueous/nonpolar interfaces. Small. 2006;2(3):413–21.
Ernst S, Heitbaum J, Hamann CH. The electrooxidation of glucose in phosphate buffer solutions: kinetics and reaction mechanism. Berichte Der Bunsengesellschaft Für Phys Chem. 1980;84(1):50–5.
Feng D, Wang F, Chen Z. Electrochemical glucose sensor based on one-step construction of gold nanoparticle–chitosan composite film. Sens Actuators B Chem. 2009;138(2):539–44.
Gao L, Zhang Q. Effects of amorphous contents and particle size on the photocatalytic properties of TiO_2 nanoparticles. Scr Mater. 2001;44(8–9):1195–8.
Govindaraj R, Pandian MS, Ramasamy P, Mukhopadhyay S. Synthesis of titanium dioxide nanostructures and their effects on current-voltage (IV) performance in dye sensitized solar cells. Int J ChemTech Res. 2014;6(13):5220–5.
Grochowska K, Ryl J, Karczewski J, Śliwiński G, Cenian A, Siuzdak K. Non-enzymatic flexible glucose sensing platform based on nanostructured TiO_2–Au composite. J Electroanal Chem. 2019;837:230–9.
Hameed RMA, Abutaleb A, Zouli N, Yousef A. Facile synthesis of electrospun transition metallic nanofibrous mats with outstanding activity for ethylene glycol electro-oxidation in alkaline solution. Mol Catal. 2022;522:112186.
Heller A, Feldman B. Electrochemical glucose sensors and their applications in diabetes management. Chem Rev. 2008;108(7):2482–505.
Hsiao MW, Adzic RR, Yeager EB. The effects of adsorbed anions on the oxidation of D-glucose on gold single crystal electrodes. Electrochim Acta. 1992;37(2):357–63.
Ismail AA, Bahnemann DW, Bannat I, Wark M. Gold nanoparticles on mesoporous interparticle networks of titanium dioxide nanocrystals for enhanced photonic efficiencies. J Phys Chem C. 2009;113(17):7429–35.
Jamil S, Fasehullah M. Effect of temperature on structure, morphology, and optical properties of TiO_2 nanoparticles. Mater Innov. 2021;1(01):22–8.
Janitabar Darzi S, Bastami H. Au decorated mesoporous TiO_2 as a high performance photocatalyst towards crystal violet dye. Adv J Chem A. 2022;5(1):22–30.
Jiang C, Wei M, Qi Z, Kudo T, Honma I, Zhou H. Particle size dependence of the lithium storage capability and high rate performance of nanocrystalline anatase TiO_2 electrode. J Power Sources. 2007;166(1):239–43.
Jin C, Chen Z. Electrocatalytic oxidation of glucose on gold–platinum nanocomposite electrodes and platinum-modified gold electrodes. Synth Met. 2007;157(13–15):592–6.
Jinga LI, Popescu-Pelin G, Socol G, Mocanu S, Tudose M, Culita DC, et al. Chemical degradation of methylene blue dye Using TiO_2/Au nanoparticles. Nanomaterials. 2021;11(6):1605.
Jovanović T, Milikić J, Cvjetićanin N, Stojadinović S, Šljukić B. Performance of Au/Ti and Au/TiO_2 nanotube array electrodes for borohydride oxidation and oxygen reduction reaction in alkaline media. Electroanalysis. 2020;32(8):1867–74.
Keswani RK, Ghodke H, Sarkar D, Khilar KC, Srinivasa RS. Room temperature synthesis of titanium dioxide nanoparticles of different phases in water in oil microemulsion. Colloids Surfaces A Physicochem Eng Asp. 2010;369(1–3):75–81.
Kibasomba PM, Dhlamini S, Maaza M, Liu C-P, Rashad MM, Rayan DA, et al. Strain and grain size of TiO_2 nanoparticles from TEM, Raman spectroscopy and XRD: The revisiting of the Williamson-Hall plot method. Results Phys. 2018;9:628–35.
Kim SH, Jung C-H, Sahu N, Park D, Yun JY, Ha H, et al. Catalytic activity of Au/TiO_2 and Pt/TiO_2 nanocatalysts prepared with arc plasma deposition under CO oxidation. Appl Catal A Gen. 2013;454:53–8.
LaConti AB, Hamdan M, McDonald RC. Handbook of fuel cells–fundamentals, technology and applications, vol. 3. New York, NY: Wiley; 2003. p. 647.
Landmann M, Rauls E, Schmidt WG. The electronic structure and optical response of rutile, anatase and brookite TiO_2. J Phys Condens Matter. 2012;24(19):195503.
Largeaud F, Kokoh KB, Beden B, Lamy C. On the electrochemical reactivity of anomers: electrocatalytic oxidation of α-and β-d-glucose on platinum electrodes in acid and basic media. J Electroanal Chem. 1995;397(1–2):261–9.
Lazar O-A, Marinoiu A, Raceanu M, Pantazi A, Mihai G, Varlam M, et al. Reduced graphene oxide decorated with dispersed gold nanoparticles: preparation, characterization and electrochemical evaluation for oxygen reduction reaction. Energies. 2020;13(17):4307.
Lertanantawong B, O'Mullane AP, Surareungchai W, Somasundrum M, Burke LD, Bond AM. Study of the underlying electrochemistry of polycrystalline gold electrodes in aqueous solution and electrocatalysis by large amplitude Fourier transformed alternating current voltammetry. Langmuir. 2008;24(6):2856–68.
Martins P, Kappert S, Le Nga H, Sebastian V, Kühn K, Alves M, et al. Enhanced photocatalytic activity of Au/TiO_2 nanoparticles against ciprofloxacin. Catalysts. 2020;10(2):234.
Meier ML. Measuring crystallite size using X-ray diffraction, the Williamson-Hall method. Department of Chemical Engineering and Materials Science, University of California, Oakland. 2005.
Moon K-S, Choi E-J, Bae J-M, Park Y-B, Oh S. Visible light-enhanced antibacterial and osteogenic functionality of Au and Pt nanoparticles deposited on TiO_2 nanotubes. Materials (basel). 2020;13(17):3721.
Ninsonti H, Chomkitichai W, Baba A, Wetchakun N, Kangwansupamonkon W, Phanichphant S, et al. Au-loaded titanium dioxide nanoparticles synthesized by modified sol-gel/impregnation methods and their application to dye-sensitized solar cells. Int J Photoenergy. 2014;2014:1–8.
Noothongkaew S, Han JK, Lee YB, Thumthan O, An K-S. Au NPs decorated TiO_2 nanotubes array candidate for UV photodetectors. Prog Nat Sci Mater Int. 2017;27(6):641–6.
Ntozakhe L, Taziwa RT, Mungondori HH. Influence of nitrogen doping on TiO_2 nanoparticles synthesized by pneumatic spray pyrolysis method. Mater Res Express. 2019;6(8):0850a9.
Ouyang L, Da G-J, Ni J, Xu J, Han Y-F. Heterogeneous catalysis by gold-based bimetallic catalysts. Recent Patents Catal. 2013;2(1):2–46.
Pan X, Xu Y-J. Fast and spontaneous reduction of gold ions over oxygen-vacancy-rich TiO_2: a novel strategy to design defect-based composite photocatalyst. Appl Catal A Gen. 2013;459:34–40.
Park S, Kim HC, Chung TD. Electrochemical analysis based on nanoporous structures. Analyst. 2012;137(17):3891–903.
Pennington AM, Pitman CL, DeSario PA, Brintlinger TH, Jeon S, Balow RB, et al. Photocatalytic CO oxidation over nanoparticulate Au-modified TiO_2 aerogels: the importance of size and intimacy. ACS Catal. 2020;10(24):14834–46.
Permana MD, Noviyanti AR, Lestari PR, Kumada N, Eddy DR, Rahayu I. Enhancing the photocatalytic activity of TiO_2/$Na_2Ti_6O_{13}$ composites by gold for the photodegradation of phenol. ChemEngineering. 2022;6(5):69.

Pisarek M, Krawczyk M, Kosiński A, Hołdyński M, Andrzejczuk M, Krajczewski J, et al. Materials characterization of TiO_2 nanotubes decorated by Au nanoparticles for photoelectrochemical applications. RSC Adv Royal Soc Chem. 2021;11(61):38727–38.
Ravishankar TN, Vaz M de O, Ramakrishnappa T, Teixeira SR, Dupont J. Ionic liquid assisted hydrothermal syntheses of Au doped TiO_2 NPs for efficient visible-light photocatalytic hydrogen production from water, electrochemical detection and photochemical detoxification of hexavalent chromium (Cr 6+). RSC Adv2017;7(68):43233–44.
Reichert R, Jusys Z, Behm RJ. Au/TiO_2 photo (electro) catalysis: the role of the Au cocatalyst in photoelectrochemical water splitting and photocatalytic H_2 evolution. J Phys Chem C. 2015;119(44):24750–9.
Romero-Torres E, Gutiérrez-Arzaluz M, Mugica-Alvarez V, González-Reyes L, Torres-Rodríguez M, Tzompantzi-Morales FJ, et al. Synthesis and characterization of gold nanoparticles on titanium dioxide for the catalytic photodegradation of 2,4-dichlorophenoxyacetic acid. J Appl Res Technol. 2018;16(5):346–56.
Senthilkumar S, Kashinath L, Ashok M, Rajendran A. Antibacterial properties and mechanism of gold nanoparticles obtained from *Pergularia Daemia* leaf extract. J Nanomed Res. 2017;6(1):00146.
Shelyapina MG, Mazur A, Yocupicio-Gaxiola RI, Caudillo-Flores U, Urtaza A, Rodionov IA, et al. Local structure of TiO_2/2D mordenite mesoporous nanocomposites probed by NMR. Appl Magn Reson. 2022;53(12):1609–20.
Sirdeshmukh DB, Sirdeshmukh L, Subhadra KG. Micro-and macro-properties of solids. Heidelberg: Springer; 2006.
Smart LE, Moore EA. Solid state chemistry: an introduction. Boca Raton: CRC Press; 2012.
Tahir M, Tahir B, Amin NAS. Gold-nanoparticle-modified TiO_2 nanowires for plasmon-enhanced photocatalytic CO_2 reduction with H_2 under visible light irradiation. Appl Surf Sci. 2015;356:1289–99.
Theivasanthi T, Alagar M. Titanium dioxide (TiO_2) nanoparticles XRD analyses: an insight. arXiv Prepr. arXiv1307.1091.2013;
Toles CA, Marshall WE, Johns MM. Surface functional groups on acid-activated nutshell carbons. Carbon N Y. 1999;37(8):1207–14.
Ungár T, Tichy G, Gubicza J, Hellmig RJ. Correlation between subgrains and coherently scattering domains. Powder Diffr. 2005;20(4):366–75.
Valour A, Cheviré F, Tessier F, Grasset F, Dierre B, Jiang T, et al. Preparation of nitrogen doped zinc oxide nanoparticles and thin films by colloidal route and low temperature nitridation process. Solid State Sci. 2016;54:30–6.
Wang G, Wei Y, Zhang W, Zhang X, Fang B, Wang L. Enzyme-free amperometric sensing of glucose using Cu-CuO nanowire composites. Microchim Acta. 2010;168(1):87–92.
Wang J, Wu S, Suo X-K, Liao H. The processes for fabricating nanopowders. In: Yang G-J, Suo X, editors. Advanced nanomaterials and coatings by thermal spray. Elsevier; 2019. p. 13–25.
Wang X, Liu X, Wang X. Self-assembly of Ag-TiO_2 nanoparticles: synthesis, characterization and catalytic application. J Wuhan Univ Technol Sci Ed. 2012;27(5):847–51.
Winjobi O, Zhang Z, Liang C, Li W. Carbon nanotube supported platinum–palladium nanoparticles for formic acid oxidation. Electrochim Acta. 2010;55(13):4217–21.
Wu Y, Liu H, Zhang J, Chen F. Enhanced photocatalytic activity of nitrogen-doped titania by deposited with gold. J Phys Chem C. 2009;113(33):14689–95.
Xiang C, Xie Q, Yao S. Electrochemical quartz crystal impedance study of glucose oxidation on a nickel hydroxide modified Au electrode in alkaline solution. Electroanal an Int J Devoted to Fundam Pract Asp Electroanal. 2003;15(11):987–90.
Xu J, Li L, Yan Y, Wang H, Wang X, Fu X, et al. Synthesis and photoluminescence of well-dispersible anatase TiO_2 nanoparticles. J Colloid Interface Sci. 2008;318(1):29–34.
Yedra L, Kumar CNS, Pshenova A, Lentzen E, Philipp P, Wirtz T, et al. A correlative method to quantitatively image trace concentrations of elements by combined SIMS-EDX analysis. J Anal at Spectrom. 2021;36(1):56–63.
Yuan Y, Ding J, Xu J, Deng J, Guo J. TiO_2 nanoparticles co-doped with silver and nitrogen for antibacterial application. J Nanosci Nanotechnol. 2010;10(8):4868–74.
Zhang D, Wen M, Zhang S, Liu P, Zhu W, Li G, et al. Au nanoparticles enhanced rutile TiO_2 nanorod bundles with high visible-light photocatalytic performance for NO oxidation. Appl Catal B Environ. 2014;147:610–6.
Zhou Y-G, Yang S, Qian Q-Y, Xia X-H. Gold nanoparticles integrated in a nanotube array for electrochemical detection of glucose. Electrochem Commun. 2009;11(1):216–9.

Publisher's Note

Springer Nature remains neutral with regard to jurisdictional claims in published maps and institutional affiliations.

Submit your manuscript to a SpringerOpen journal and benefit from:

- ► Convenient online submission
- ► Rigorous peer review
- ► Open access: articles freely available online
- ► High visibility within the field
- ► Retaining the copyright to your article

Submit your next manuscript at ► springeropen.com